Supplementary Information

Excitation Generated Preferential Binding Sites for Ethane on Porous Carbon-Copper Porphyrin Sorbents: Ethane/Ethylene Adsorptive Separation Improved by Light

Shi-Chao Qi, Yun-Jie Zhao, Xiao-Jie Lu, Yong-Lan Liu, Zhen Sun, Xiao-Qin Liu and Lin-Bing Sun*

State Key Laboratory of Materials-Oriented Chemical Engineering, Jiangsu National Synergetic Innovation Center for Advanced Materials (SICAM), College of Chemical Engineering, Nanjing Tech University, 211816, Nanjing, China

*E-mail: lbsun@njtech.edu.cn

Experimental and computational procedures

Materials synthesis

All chemicals were commercially purchased and used as received. The TCPP (purity, > 95%) was purchased from Jilin Chinese Academy of Sciences - Yanshen Technology Co., Ltd. The MC (purity: C.P.) and HC (purity: C.P.) powder was provided by the Adamas Co., Ltd., and Jiangsu Xianfeng Nano Material Technology Co., Ltd., respectively. The pristine CuT was synthesized as follows. Under the N_2 protection, the TCPP (100 mg) and $CuCl_2 \cdot 2H_2O$ (65 mg) were dissolved in a mixture of *N*,*N*-dimethylformamide (DMF, 20 mL) and ethanol (5 mL), with vigorous stirring at 80 °C for 5 h. After cooling down to the ambient temperature, the CuT was harvested by centrifugation, and then successively washed with ethanol. The composite materials were prepared as follows. Under the N_2 protection, the MC or HC powder (100 mg) and the CuT (80 mg) were ultrasonically dispersed in the mixture of DMF (20 mL) and ethanol (5 mL), followed by vigorous stirring at 80 °C for 6 h, and then the suspension underwent freeze-drying to harvest the purple-black powder CuT/MC or CuT/HC, correspondingly. The reference composite sorbents of *x*CuT/MC and *x*CuT/HC were prepared with the same recipe, while the mass of CuT dispersed was 10, 20, or 40 mg for x = 0.1, 0.2, or 0.4, correspondingly.

Characterization methods

The SEM images were scanned on a ZEISS Sigma500 microscope with a Bruker 60 EDS. The HREM images were observed on a JEM-2100F apparatus at an accelerating voltage of 200 kV. With Cu Kα at 40 kV and 40 mA, the XRPD patterns were tested with a Bruker D8 Advance diffractometer. With the KBr wafer, a Nicolet Nexus 470 spectrometer was used to record the FTIR spectra. The XPS was recorded on a Thermo Scientific Escalab 250Xi device with an Al Kα source. TG analyses in N_2 atmosphere were performed with a TG209F1 apparatus. The liquid UV-Vis absorption spectra and the phosphor decay profiles were recorded at ambient temperature with an FLS1000 from Edinburgh Instruments. After degassing the materials at 110 °C for 5 h, the N_2 adsorption-desorption isotherms at 77 K were measured over a Micromeritics ASAP 2020 analyzer. The BET specific surface areas were calculated at the P/P_0 range of 0.05–0.15. The total pore volumes were calculated at the relative pressure of 0.95, and the non-local density functional theory (NLDFT) was used to estimate the pore size distribution.

Adsorption experiments

Static adsorption experiments of C_2H_6 (purity, > 99.999%) or C_2H_4 (purity, > 99.999%) were measured with the Micromeritics ASAP 2020 analyzer. The free space was determined using helium (purity, > 99.999%), with the assumption that the helium was not adsorbed. For pristine tests, the adsorption isotherms were obtained in a dark environment, with the sample cells immersed in an ice-water bath of 0 °C. For the Vis radiation tests, a CEL-HXUV300 xenon lamp (optical power density: 2,000 mW cm^{-2}; Beijing China Education AuLight Technology Co., Ltd.) was used with a QD420 optical filter to generate the light at 420 nm. The xenon lamp was placed 20 cm away from the sample cells to provide excitation light source, and other operation conditions were same to the pristine ones.

Dual-Langmuir model was employed to fit the adsorption isotherms (Eq. S1), and the fitting parameters are given in Table S4. The ideal adsorption solution theory (IAST) was then used for evaluating the adsorption selectivity of binary gas separation (Eq. S2 and S3).

$$q = q_1 \frac{k_1 P}{1 + k_1 P} + q_2 \frac{k_2 P}{1 + k_2 P} \tag{S1}$$

in which the subscripts of 1 and 2 represent two types of adsorption sites, respectively; q (mmol g^{-1}) gives the total adsorption capacity; q_1 or q_2 (mmol g^{-1}) represents the maximum adsorption capacity; k (bar^{-1}) means the Langmuir equilibrium constant; P (bar) is the system pressure; R^2 is the fitting correlation coefficient.

$$q_{1i} \ln\left(1 + \frac{k_{1i} y_i P}{x_i}\right) - q_{1j} \ln\left[1 + \frac{k_{1j}(1 - y_i)P}{1 - x_i}\right] + q_{2i} \ln\left(1 + \frac{k_{2i} y_i P}{x_i}\right) - q_{2j} ln\left[1 + \frac{k_{2j}(1 - y_i)P}{1 - x_i}\right] = 0 \tag{S2}$$

where q_{1i}, k_{1i}, q_{2i}, and k_{2i} are the Langmuir parameters of component i calculated from Eq. S1, and correspondingly, q_{1j}, k_{1j}, q_{2j}, and k_{2j} are the Langmuir parameters of component j ; P is the system pressure.

$$Selectivity = \frac{x_i / x_j}{y_i / y_j} \tag{S3}$$

where x_i and y_i (x_j and y_j) are the molar fractions of component i (component j) in the adsorbed and bulk phase, respectively.

Dynamic breakthrough experiments were performed in a quartz tube with an internal diameter of 4 mm and length of 150 mm, packed with 500 mg sample. Helium was used to purge the sample at 100 °C for 6 h. After the sample cooled down, the tube was then immersed in an ice-water bath of 0 ºC. The gas mixture of C_2H_6/C_2H_4 (10/90, v/v) was employed as the feedstock, with the flow rate of 2 mL/min. For pristine experiments, the experiments were carried out in the darkness, and the gas mixture was detected by a gas chromatograph of SP-6890 after adsorption. For the Vis radiation experiments, the illumination was operated as that of the static adsorption experiments.

Computational methods

The DFT calculations were carried out with Vienna Ab-initio Simulation Package (VASP, 5.4 release). The generalized gradient approximation of Perdew-Burke-Ernzerhof functional was employed to describe the electronic exchange and correlation, and Grimme's dispersion correction of D3BJ version was employed to correct the London forces. The plane wave pseudopotential with a kinetic cutoff energy of 400 eV within the projector augmented wave (PAW) method was used. The Gaussian smearing method with a smearing width of 0.001 eV was adopted, with the spin-polarized self-consistent field convergence criteria of energy < 1×10^{-4} a.u.. The ionic relaxation was carried out with the break condition of force < 0.02 eV $Å^{-1}$, with the Γ-point in view of the large enough supercells. For the calculations on the electron excitation, the transmission of the frontline electron to the minimum empty band was implemented, which was kept fixed throughout the computation, and all the convergence criteria were identical with those of the ground states.

Based on the DFT calculation, the adsorption binding energy (ABE) is defined according to Eq. S3, in which the GS means the ground state and the ES means the excited state. The electrons of C_2H_4 and C_2H_6 cannot be excited with the Vis radiation, so only the GS of the gas molecule is involved herein.

$$ABE_{GS} = E_{GS}\,(\text{Sorbent-Gas}) - E_{GS}\,(\text{Sorbent}) - E_{GS}\,(\text{Gas})$$
$$ABE_{ES} = E_{ES}\,(\text{Sorbent-Gas}) - E_{ES}\,(\text{Sorbent}) - E_{GS}\,(\text{Gas}) \quad \text{(S3)}$$

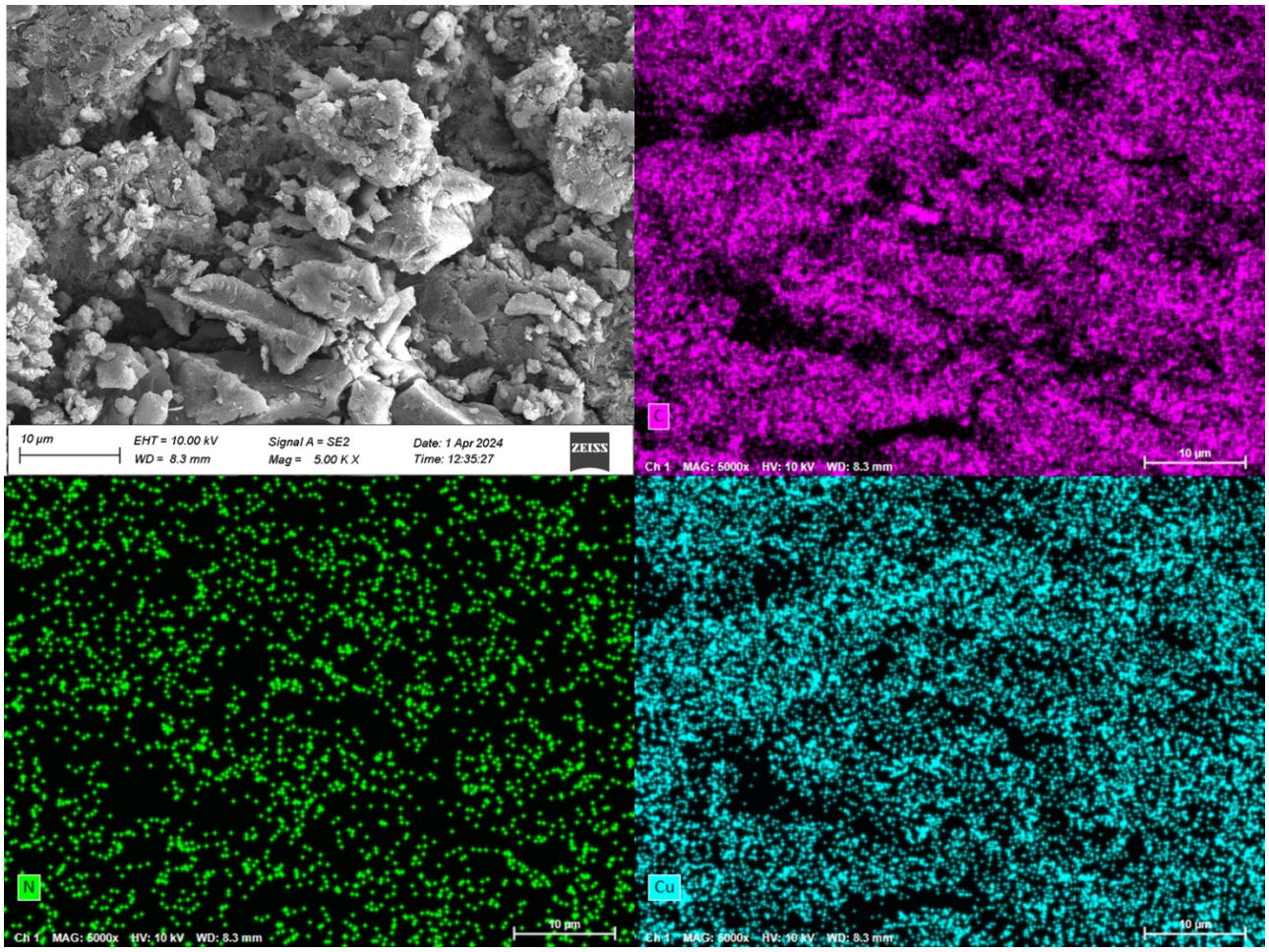

Fig. S1 The SEM and EDS images of the pristine CuT.

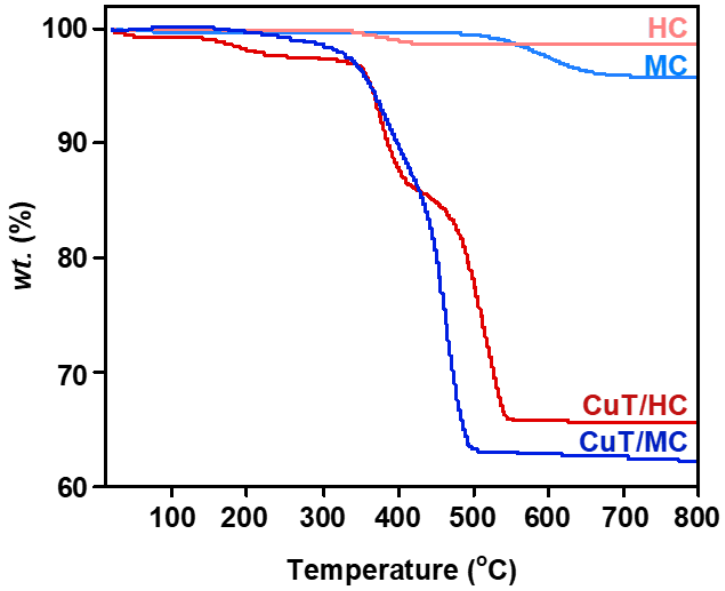

Fig. S2 The TG profiles of the composite sorbents and their host materials.

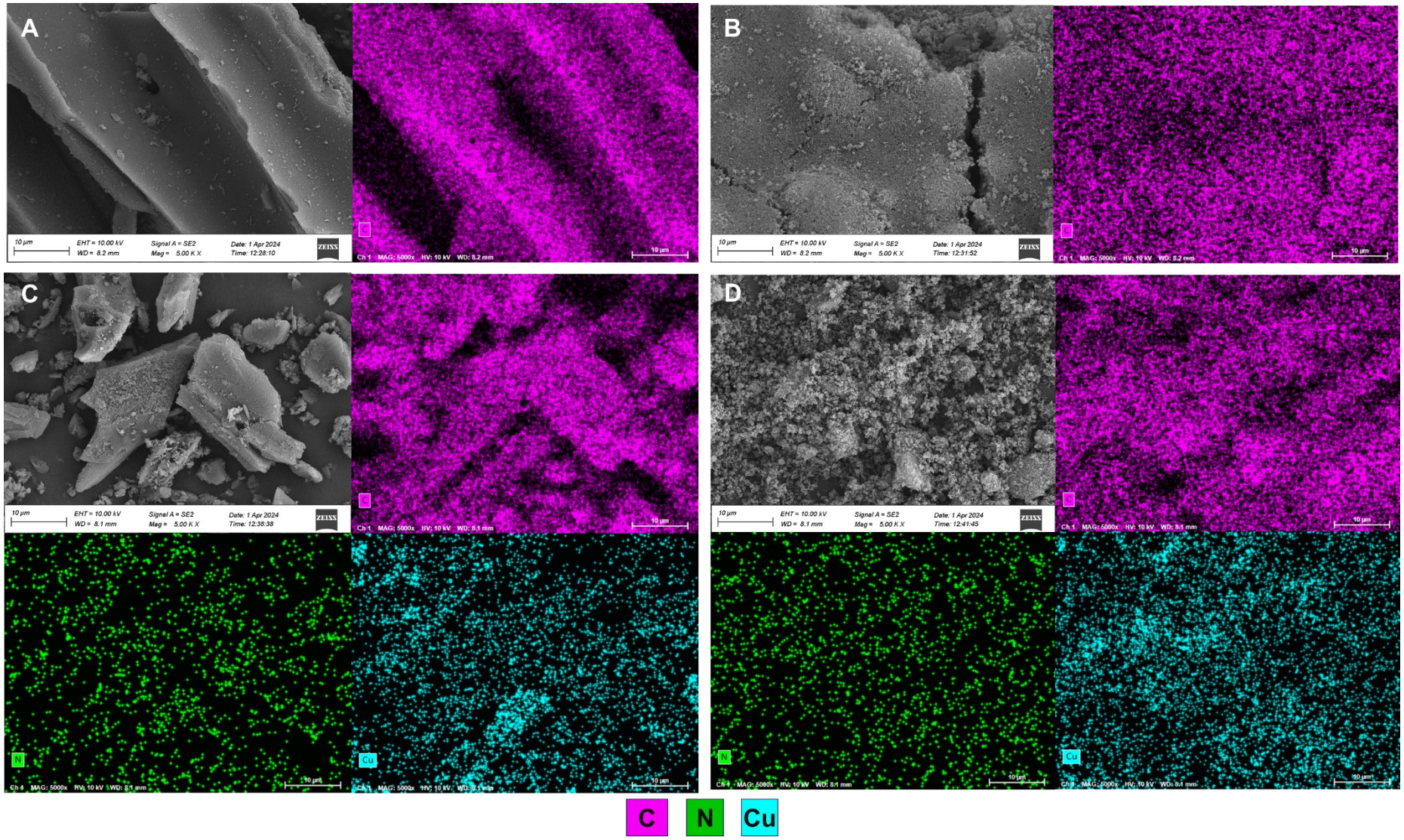

Fig. S3 The SEM and EDS images of the composite sorbents and their host materials. (A), MC; (B), HC; (C), CuT/MC; (D), CuT/HC.

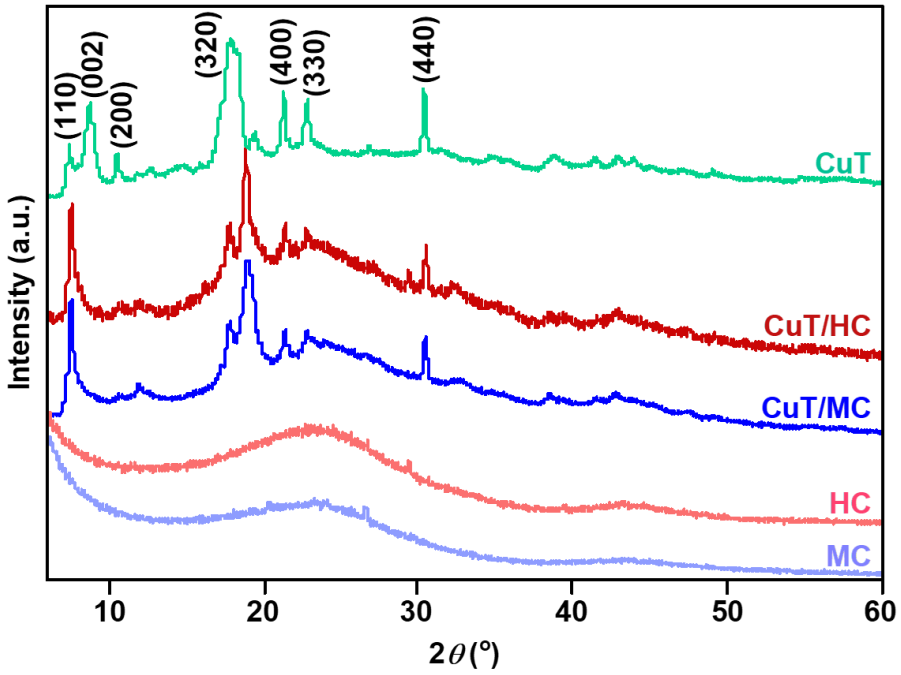

Fig. S4 The XRPD patterns of the pristine and composite materials.

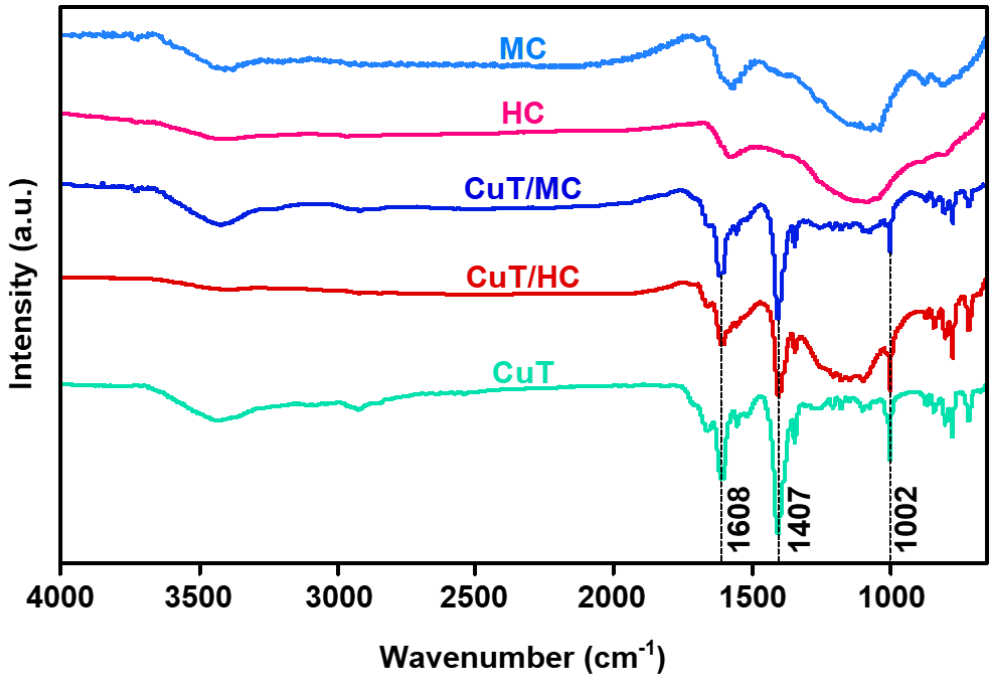

Fig. S5 The FTIR patterns of the pristine and composite materials.

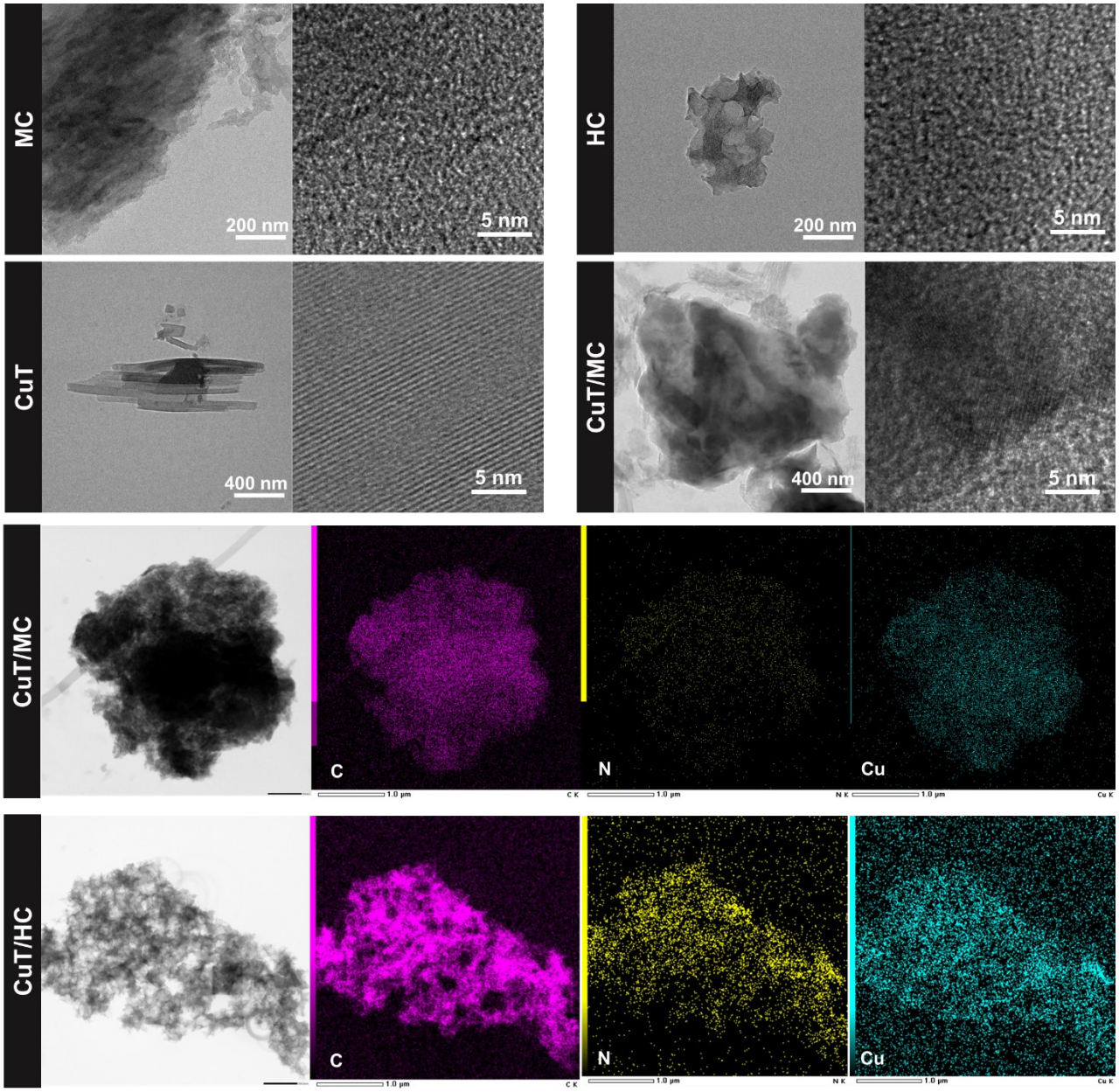

Fig. S6 The HREM images of MC, HC, CuT, and CuT/MC, and the elemental mappings of C, N, Cu for CuT/MC and CuT/HC.

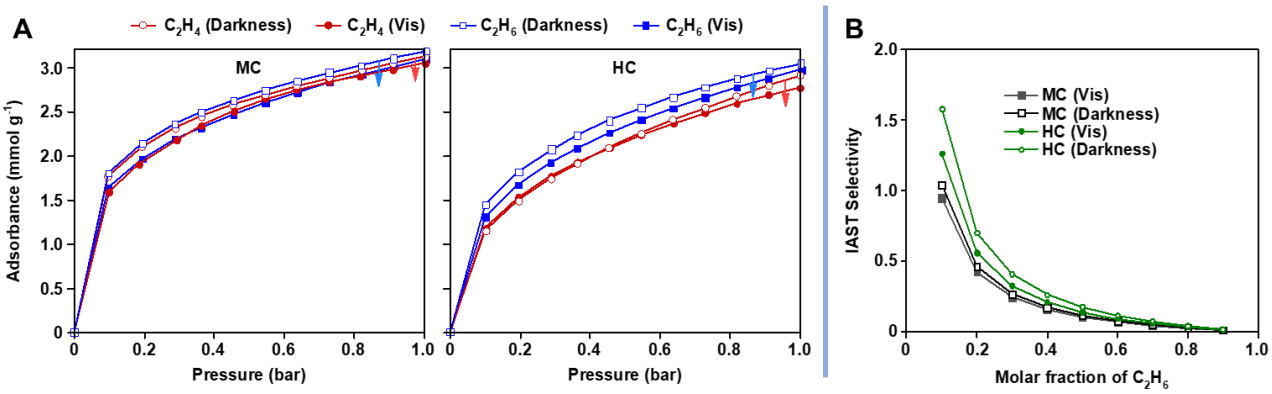

Fig. S7 The static adsorption results of C_2H_4 and C_2H_6 over MC and HC at 0 °C. A) The static adsorption isotherms, of which the blue arrow indicates the variation trend of the C_2H_6 adsorption isotherm under the Vis radiation with respect to that in the darkness, and the red arrow shows the variation trend of the C_2H_4 adsorption isotherm. B) The calculated IAST selectivity at 0 °C and 1 bar on the variable of the molar fraction of C_2H_6.

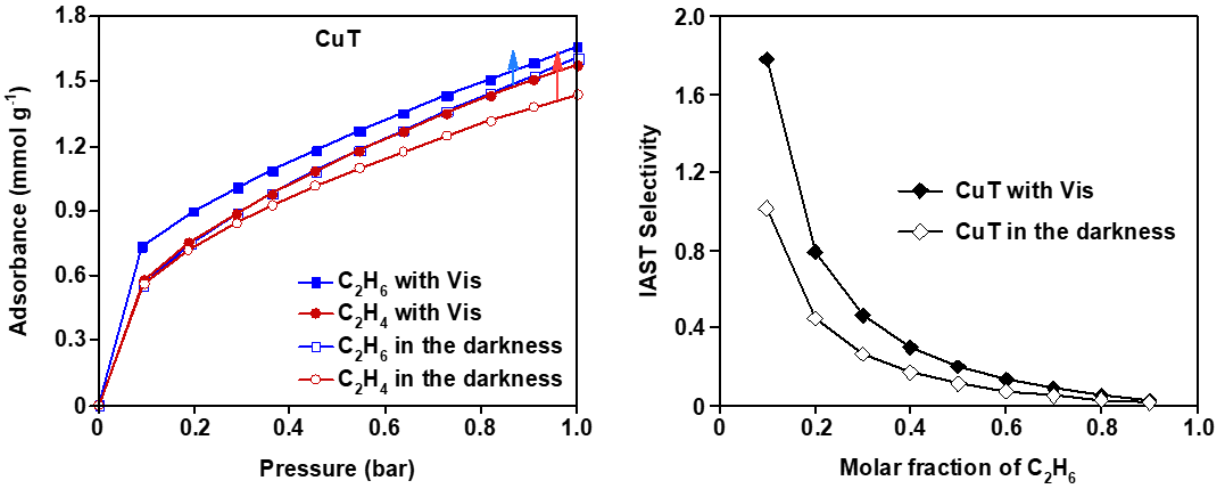

Fig. S8 The static adsorption isotherms of C_2H_6 and C_2H_4 tested with the Vis radiation and in the darkness over the pristine CuT at 0 °C, and the calculated IAST selectivity at 0 °C and 1 bar on the variable of the molar fraction of C_2H_6. The blue arrow indicates the variation trend of the C_2H_6 adsorption isotherm under the Vis radiation with respect to that in the darkness, and the red arrow show the variation trend of the C_2H_4 adsorption isotherm.

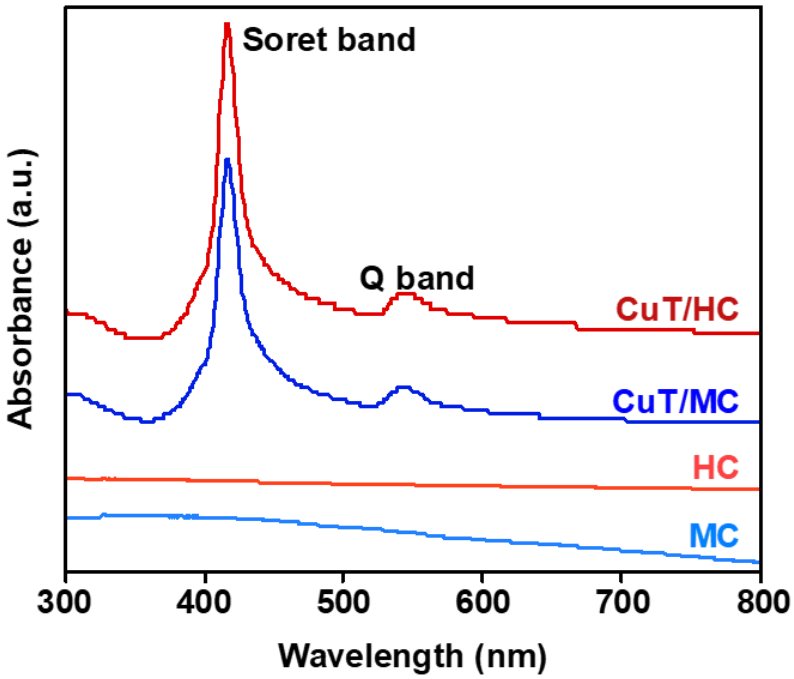

Fig. S9 The liquid UV-Vis absorption bands of the composite sorbents and their host materials.

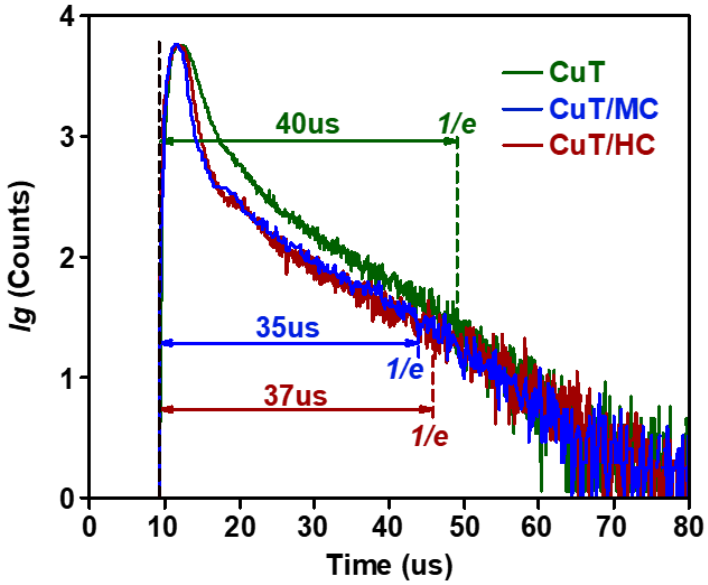

Fig. S10 The phosphor decay profiles for CuT, CuT/MC, and CuT/HC excited by Vis at 420 nm.

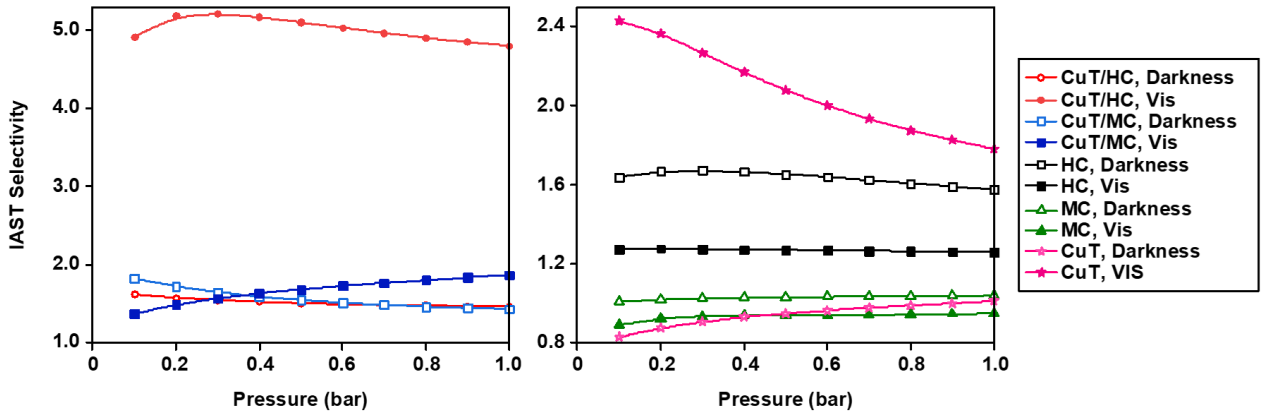

Fig. S11 The calculated IAST selectivity (C_2H_6/C_2H_4 = 10/90, v/v) of the pristine and composite materials at 0 °C on the variable of the pressure.

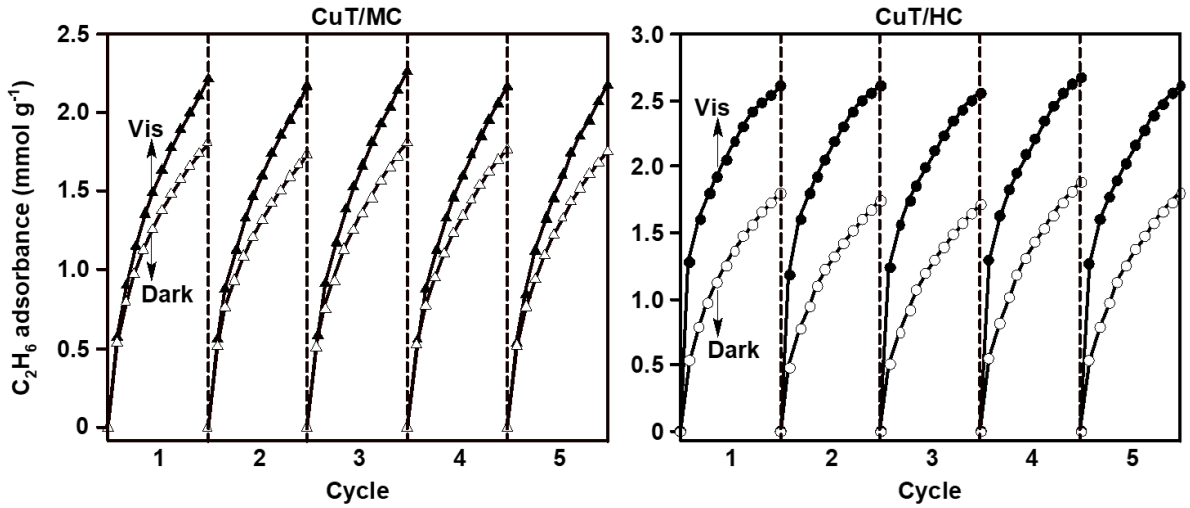

Fig. S12 The recyclability tests for the CuT/MC and CuT/HC.

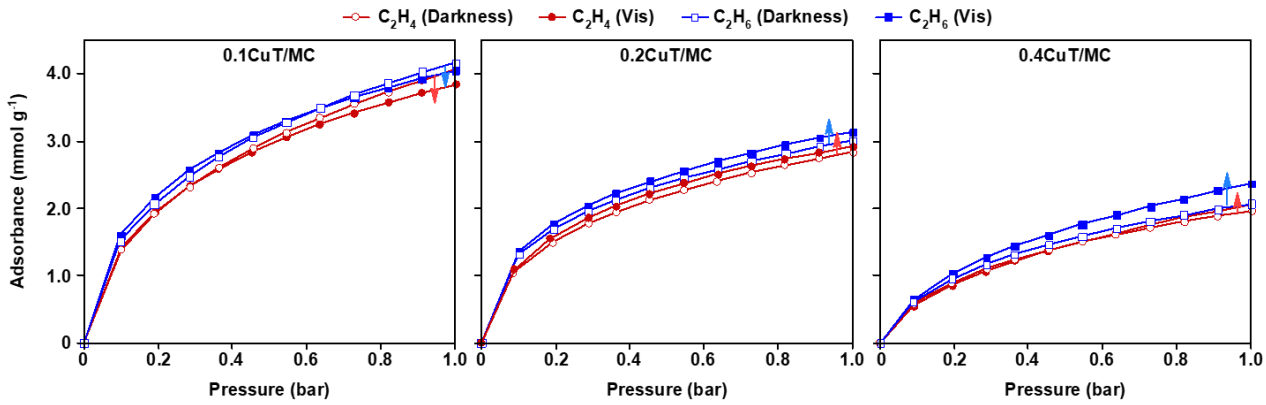

Fig. S13 The static adsorption results of C_2H_4 and C_2H_6 over the reference *x*CuT/MC (*x* = 0.1, 0.2, or 0.4) at 0 °C, of which the blue arrow indicates the variation trend of the C_2H_6 adsorption isotherm under the Vis radiation with respect to that in the darkness, and the red arrow shows the variation trend of the C_2H_4 adsorption isotherm.

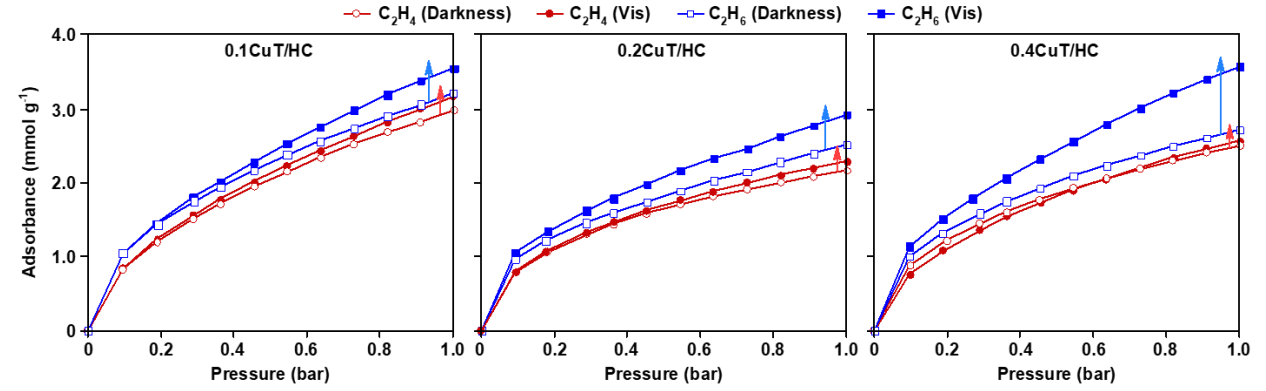

Fig. S14 The static adsorption results of C_2H_4 and C_2H_6 over the reference *x*CuT/HC (*x* = 0.1, 0.2, or 0.4) at 0 °C, of which the blue arrow indicates the variation trend of the C_2H_6 adsorption isotherm under the Vis radiation with respect to that in the darkness, and the red arrow shows the variation trend of the C_2H_4 adsorption isotherm.

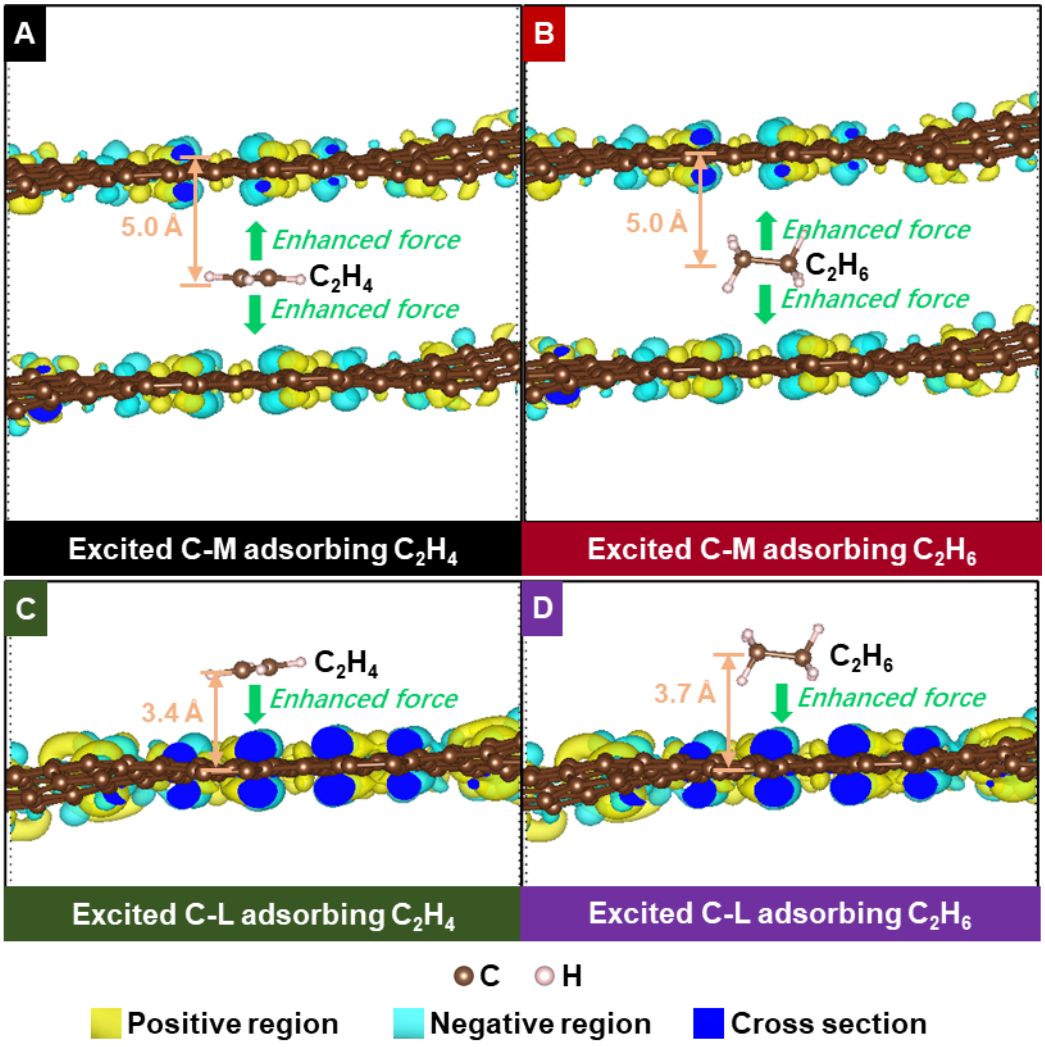

Fig. S15 The DCD images of the excited carbonaceous sites adsorbing C_2H_4 and C_2H_6 with respect to their ground states. DCD = CD (excited state) − CD (ground state); DCD: differential charge density; CD: charge density. A) and B): the DCD images of the excited C-M site respectively adsorbing C_2H_4 and C_2H_6, in which the C-M simulates the micropore structures in the carbonaceous sorbent, constructed *via* locating two carbon layers with the *c*-axial distance of 1 nm. C) and D): the DCD images of the excited C-L site respectively adsorbing C_2H_4 and C_2H_6, in which the C-L simulates the mesopore and large pore structures in the carbonaceous sorbent, constructed with a carbon layer.

Table S1. The textural properties of the sorbents and the adsorption capabilities at 0 °C and 1 bar.

Sorbent	S_{BET}	$V_{total\ pore}$	$V_{micropore}$	C_2H_4 uptake	C_2H_6 uptake	IAST selectivity (C_2H_6)	
	$m^2\ g^{-1}$	$cm^3\ g^{-1}$	$cm^3\ g^{-1}$	mmol g^{-1}	mmol g^{-1}	*Darkness*	*Vis*
CuT/HC	400	0.63	0.10	1.67 / 1.70 [a]	2.06 / 2.62	1.5	4.8
CuT/MC	790	0.60	0.21	1.75 / 1.91	1.80 / 2.21	1.4	1.9
HC	640	1.04	0.27	2.92 / 2.77	3.04 / 2.98	1.6	1.3
MC	1020	0.79	0.30	3.12 / 3.05	3.18 / 3.10	1.0	0.9
CuT	30	--	--	1.44 / 1.58	1.61 / 1.66	1.0	1.8

a, the adsorption capacity in the darkness / the adsorption capacity with Vis.

Table S2. The C_2H_6 and C_2H_4 adsorption capabilities of some representative benchmark sorbents.

Sorbent	S_{BET} ($m^2\ g^{-1}$)	Adsorption capacity at 1 bar		IAST C_2H_6-selectivity	Refs.
		C_2H_4 (mmol g^{-1})	C_2H_6 (mmol g^{-1})		
CuT/HC	400	1.70	2.62	4.8	This work
CuT/MC	790	1.91	2.21	1.9	This work
$Fe_2(O_2)$(dobdc)	1073	2.52	3.32	4.4	18
NbU-12	2053	2.50	3.67	1.5	19
$Zn_4O(NTB)_2$	529	2.45	2.83	2.1	S1
BUT-151	1330	5.20	5.80	1.4	S2
LIFM-63	1486	3.70	4.80	1.6	S3
PAN-AN	955	3.27	3.81	1.7	S4
MCM-41	795	1.28	1.45	1.0	S5
CPOC-301	1962	4.54	5.50	1.3	S6
Tb-MOF-76	--	3.50	3.60	1.7	S7
Sm-BTC	700	1.56	1.65	1.7	S8
UiO-66-2CF_3	467	0.49	0.88	2.5	S9
$CuIn(ina)_4$	639	3.30	3.05	2.3	S10
ZIF-4	300	2.20	2.30	2.2	S11
ZJU-HOF-10	1169	1.88	2.19	1.9	S12

Table S3. The adsorption binding energy (ABE) values of C_2H_4 and C_2H_6 over different model sites at ground state (GS) and at excited state (ES).

Model site	Gas	ABE, GS	ABE, ES	Model site	Gas	ABE, GS	ABE, ES
		kJ/mol	kJ/mol			kJ/mol	kJ/mol
CP-M	C_2H_4	-47	-46	C-M	C_2H_4	-36	-36
CP-M	C_2H_6	-49	-63	C-M	C_2H_6	-39	-39
CP-L	C_2H_4	-26	-26	C-L	C_2H_4	-19	-19
CP-L	C_2H_6	-20	-25	C-L	C_2H_6	-19	-19

Table S4. The adsorption binding energy (ABE) values of C_2H_4 and C_2H_6 over monolayer or bilayer CuT frameworks at ground state.

Model site	Gas	ABE kJ/mol	Image	Model site	Gas	ABE kJ/mol	Image
Monolayer	C_2H_4	-29	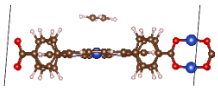	Monolayer	C_2H_6	-12	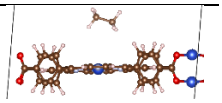
Bilayer	C_2H_4	-21	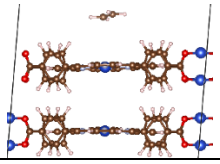	Bilayer	C_2H_6	-40	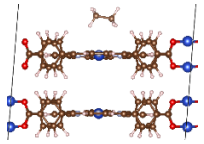

Table S5. The parameters of Dual-Langmuir model fitting the adsorption isotherms.

Sorbent	Condition	Adsorbate	q_1	k_1	q_2	k_2	R^2
			mmol g^{-1}	bar^{-1}	mmol g^{-1}	bar^{-1}	
CuT/HC	Darkness	C_2H_6	0.7966	35.6596	3.0745	0.5600	1.000
CuT/HC	Darkness	C_2H_4	2.5895	0.5380	0.7979	20.6531	0.999
CuT/HC	Vis	C_2H_6	1.1049	60.5878	2.8049	1.1478	0.999
CuT/HC	Vis	C_2H_4	2.6247	0.8021	0.5432	31.5809	0.999
CuT/MC	Darkness	C_2H_6	0.7666	20.6596	3.0745	0.5600	1.000
CuT/MC	Darkness	C_2H_4	0.7655	9.4696	2.9044	0.5711	1.000
CuT/MC	Vis	C_2H_6	54.4698	0.0387	1.5752	4.6121	0.999
CuT/MC	Vis	C_2H_4	0.5699	10.0340	3.6712	0.6068	0.999
HC	Darkness	C_2H_6	3.1401	0.9639	1.5523	29.7321	0.999
HC	Darkness	C_2H_4	1.3079	22.8869	5.5314	0.4288	0.999
HC	Vis	C_2H_6	3.8970	0.6839	1.4429	26.7581	0.999
HC	Vis	C_2H_4	3.8236	0.6181	1.3767	22.1448	0.999
MC	Darkness	C_2H_6	2.0473	38.0951	2.8842	0.6959	0.999
MC	Darkness	C_2H_4	2.0002	39.6472	2.8548	0.69034	0.999
MC	Vis	C_2H_6	1.7910	41.7810	3.5550	0.6101	0.999
MC	Vis	C_2H_4	1.3049	82.0408	2.7219	1.8211	0.999
CuT	Darkness	C_2H_6	5.6977	0.2093	0.6451	23.4164	0.999
CuT	Darkness	C_2H_4	0.5800	36.1986	3.0868	0.3960	0.999
CuT	Vis	C_2H_6	0.7294	73.3182	5.3239	0.2146	0.999
CuT	Vis	C_2H_4	0.5684	40.8326	3.8371	0.3635	0.999

References

[S1] Y. Zhang, S. Y. Zhou, X. Liu, P. X. Zhang, Z. H. Yan, J. G. Hu, Z. Q. Wei, L. H. Chen, J. Wang and S. G. Deng, *Sep. Purif. Technol.*, 2022, **301**, 122011.

[S2] H. T. Wang, Q. Chen, X. Zhang, Y. L. Zhao, M. M. Xu, R. B. Lin, H. L. Huang, L. H. Xie and J.

R. Li, *J. Mater. Chem. A*, 2022, **10**, 12497-12502.

[S3] C. X. Chen, Z. W. Wei, T. Pham, P. C. Lan, L. Zhang, K. A. Forrest, S. Chen, A. M. Al-Enizi, A. Nafady, C. Y. Su and S. Q. Ma, *Angew. Chem. Int. Ed.*, 2021, **60**, 9680-9685.

[S4] C. H. Wang, J. Yan, Z. C. Ma and Z. G. Wang, *Sep. Purif. Technol.*, 2022, **287**, 120580.

[S5] F. Anwar, K. S. K. Reddy, A. M. Varghese, M. Khaleel, K. Wang and G. N. Karanikolos, *Sep. Purif. Technol.*, 2023, **323**, 124324.

[S6] K. Z. Su, W. J. Wang, S. F. Du, C. Q. Ji and D. Q. Yuan, Efficient ethylene purification by a robust ethane-trapping porous organic cage. *Nat. Commun.*, 2021, **12**, 3703.

[S7] G. D. Wang, R. Krishna, Y. Z. Li, W. J. Shi, L. Hou, Y. Y. Wang and Z. H. Zhu, *Angew. Chem. Int. Ed.*, 2022, **61**, e202213015.

[S8] C. H. He, Y. Wang, Y. Chen, X. Q. Wang, J. F. Yang, L. B. Li and J. P. Li, *Ind. Eng. Chem. Res.*, 2020, **59**, 6123-6129.

[S9] J. Pires, J. Fernandes, K. Dedecker, J. R. B. Gomes, G. Pérez-Sánchez, F. Nouar, C. Serre and M. L. Pinto, *ACS Appl. Mater. Interfaces*, 2019, **11**, 27410-27421.

[S10] L. Yang, Q. Gao, Y. M. Zhang, R. H. Wang and L. Z. Chen, *J. Colloid Interface Sci.*, 2023, **652**, 1093-1098.

[S11] M. Hartmann, U. Böhme, M. Hovestadt and C. Paula, *Langmuir*, 2015, **31**, 12382-12389.

[S12] J. X. Wang, X. W. Gu, Y. X. Lin, B. Li and G. D. Qian, *ACS Materials Lett.*, 2021, **3**, 497-503.